AGU PUBLICATIONS

Geophysical Research Letters

RESEARCH LETTER
10.1002/2017GL075283

Key Points:
- Experimentally determined Mg partitioning between iron-rich liquid and silicate melt
- Mg partitioning depends strongly on the oxygen content in iron-rich liquid
- MgO exsolution during core cooling is drastically reduced and insufficient to drive an early geodynamo alone

Supporting Information:
- Supporting Information S1

Correspondence to:
Z. Du,
zdu@carnegiescience.edu

Citation:
Du, Z., Jackson, C., Bennett, N., Driscoll, P., Deng, J., Lee, K. K. M., … Fei, Y. (2017). Insufficient energy from MgO exsolution to power early geodynamo. *Geophysical Research Letters*, *44*. https://doi.org/10.1002/2017GL075283

Received 11 AUG 2017
Accepted 10 NOV 2017
Accepted article online 13 NOV 2017

Insufficient Energy From MgO Exsolution to Power Early Geodynamo

Zhixue Du[1], Colin Jackson[1,2], Neil Bennett[1], Peter Driscoll[3], Jie Deng[4], Kanani K. M. Lee[4], Eran Greenberg[5], Vitali B. Prakapenka[5], and Yingwei Fei[1]

[1]Geophysical Laboratory, Carnegie Institution of Washington, Washington, DC, USA, [2]National Museum of Natural History, Smithsonian Institution, Washington, DC, USA, [3]Department of Terrestrial Magnetism, Carnegie Institution of Washington, Washington, DC, USA, [4]Department of Geology and Geophysics, Yale University, New Haven, CT, USA, [5]Center for Advanced Radiation Sources, University of Chicago, Chicago, IL, USA

Abstract The origin of Earth's ancient magnetic field is an outstanding problem. It has recently been proposed that exsolution of MgO from the core may provide sufficient energy to drive an early geodynamo. Here we present new experiments on Mg partitioning between iron-rich liquids and silicate/oxide melts. Our results indicate that Mg partitioning depends strongly on the oxygen content in the iron-rich liquid, in contrast to previous findings that it depends only on temperature. Consequently, MgO exsolution during core cooling is drastically reduced and insufficient to drive an early geodynamo alone. Using the new experimental data, our thermal model predicts inner core nucleation at ~850 Ma and a nearly constant paleointensity.

1. Introduction

Paleomagnetic evidence suggests that the terrestrial magnetic field has persisted since early in Earth's history (Biggin et al., 2015; Tarduno et al., 2015). However, the energetics of the Earth and newly refined thermal conductivity values for the core (de Koker et al., 2012; Pozzo et al., 2012) appear to preclude an early dynamo. Although the thermal conductivity of the core remains controversial (Konopkova et al., 2016; Ohta et al., 2016), several mechanisms have now been proposed to resolve this "new core paradox" (Olson, 2013), including a large amount of core radioactivity (Driscoll & Bercovici, 2014) or exsolution of MgO (Badro et al., 2016; O'Rourke & Stevenson, 2016) or SiO_2 (Hirose et al., 2017). The work of the MgO exsolution model during core cooling (Badro et al., 2016; O'Rourke & Stevenson, 2016) relies on an apparent strong temperature dependence of the metal-silicate partitioning of Mg. However, controlling factors on the metal-silicate partitioning of Mg are not fully understood. Here we provide a new suite of experimental data on the partitioning of Mg between liquid iron and silicate or oxide melts that reveal crucial compositional dependence. The results show that temperature has a limited effect on MgO exsolution and therefore cannot provide necessary power alone to drive the early geodynamo.

2. Materials and Methods

Our experiments consist of metal-silicate partitioning experiments under Earth's core formation conditions using a laser-heated diamond-anvil cell. Mantle and core materials in the experiments are represented by pyrolite (or basalt, ferropericlase) and Fe (or FeSi alloy, or Fe-FeS mixture), respectively. These materials are equilibrated at temperatures and pressures of 3000–5000 K and 20–66 gigapascal (GPa). Melting is identified in situ by the appearance of a diffuse signal in X-ray diffraction patterns (Figure S1) and then confirmed ex situ from the textural appearance of recovered run products (Figure S2). Where melting has occurred, heated spot are composed of an iron-rich metallic bleb surrounded by a quenched silicate/oxide melt (Figure S2). Quenched melt spots are exposed for analysis by focused-ion-beam milling and composition characterized using a field-emission electron microprobe (FE-EMP) with a spatial resolution of ~1 μm (supporting information).

The reaction between MgO in the silicate melt and iron-rich liquid can be described as follows:

$$MgO^{silicate\ melt} + Fe^{metal} \rightleftharpoons FeO^{silicate\ melt} + Mg^{metal} \quad (1)$$

The exchange coefficient for the reaction above is defined as: $K_{Mg} = X_{FeO}X_{Mg}/(X_{Fe}X_{MgO})$, where X_{FeO} and X_{MgO} are the mole fraction of FeO and MgO component in silicate melt, respectively, while X_{Mg}, X_{Fe} are the Fe, Mg components in iron-rich liquid metal, respectively.

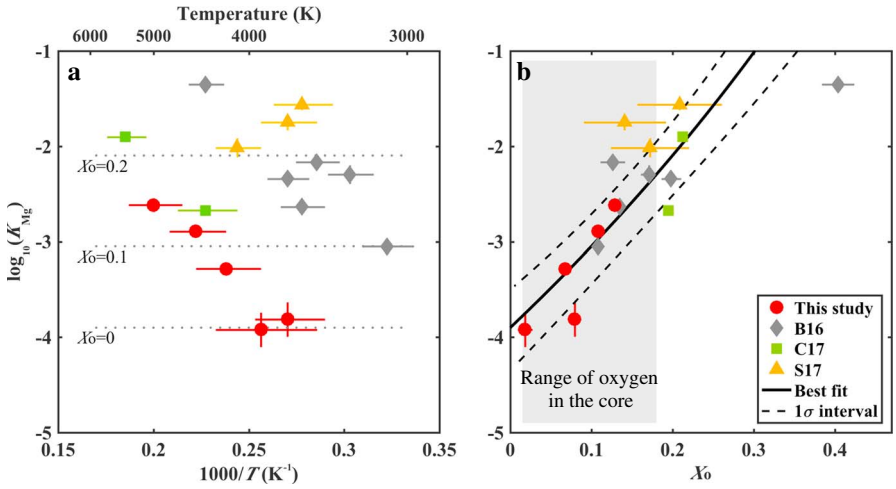

Figure 1. Exchange coefficient (K_{Mg}) as a function of (a) reciprocal temperature (1,000/T) and (b) X_O, oxygen content in iron-rich liquid metal (mole fraction) in red circles (this study), gray diamonds (B16) (Badro et al., 2016), green squares (C17) (Chidester et al., 2017), and yellow triangles (S17) (Suer et al., 2017). Experimental data for this study are shown in Extended Data Table S1. Error bars correspond to 1σ experimental uncertainties. In Figure 1a, contours of K_{Mg} at X_O = 0, 0.1, 0.2, are shown in gray dotted lines. In Figure 1b, the best fit line from weighted linear least squares fit and the 1σ confidence interval are shown in solid and dashed curves, respectively. The range of estimates for the oxygen content in the core is shown in the shaded region (e.g., Badro et al., 2015; Fischer et al., 2015; Huang et al., 2011; O'Rourke & Stevenson, 2016; Rubie et al., 2011; Wade & Wood, 2005). Also note that the experiment "16cc33C" is not plotted because Mg content in iron-rich liquid is below detection limit.

3. Data

The measured K_{Mg} values from our experiments (Table S1) are much lower at a given temperature than the previous studies of (Badro et al., 2016) and (Suer et al., 2017) but consistent with (Chidester et al., 2017) (referred to as BS16, S17, and C17, respectively) (Figure 1a). Moreover, for our results alone, we find that K_{Mg} is positively correlated with temperature, which is also the case for each individual study (Badro et al., 2016; Chidester et al., 2017; Suer et al., 2017). There are major discrepancies, however, between this study and previous studies (Badro et al., 2016; Suer et al., 2017). It is possible some of this discrepancy could be associated with uncertainties in the temperature measurement (Deng et al., 2017), but either systematic temperature overestimation (Badro et al., 2016; Suer et al., 2017) or temperature underestimation (this study; (Chidester et al., 2017)) by at least 1200 K is required to reconcile the discrepancy. On the other hand, Figure 1b reveals a strong correlation between the K_{Mg} and oxygen content in the iron-rich liquid (X_O) among all studies without invoking temperature discrepancy. This suggests that K_{Mg} must strongly depend on X_O rather than temperature alone.

4. Results

Following the previous approach (Ma, 2001) and considering the low concentration of Mg ($X_{Mg} < 0.01$), we neglect the self-interaction term and higher than first-order terms and therefore K_{Mg} can be parameterized as follows:

$$\log_{10}(K_{Mg}) = a + b/T + cP/T + d\log_{10}(1 - X_O)$$

where T is temperature in kelvin and P is pressure in GPa; X_O is the mole fraction of oxygen in the iron-rich liquid. Parameters a, b, c, and d are determined from a weighted linear least squares fit to our combined data set (supporting information). We note that the interaction parameter d is assumed to be a constant in our regression, unlike some previous studies where the interaction parameters are inversely proportional to temperature (e.g., Wade & Wood, 2005). We then regress the data set including those from this study (Table S1) and previous studies (Badro et al., 2016; Chidester et al., 2017; Suer et al., 2017). It yields:

$$\log_{10}(K_{Mg}) = -3.9(0.2) - 18.6(2)\log_{10}(1 - X_O)$$

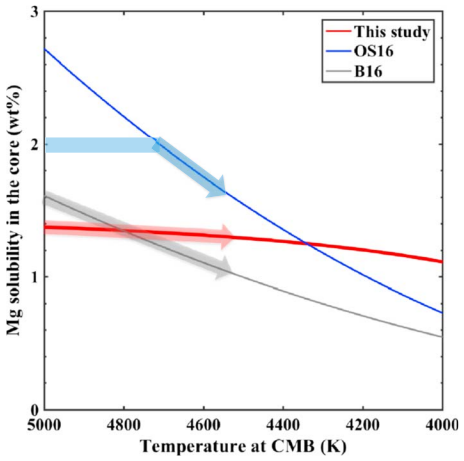

Figure 2. Calculated Mg solubility in the Earth's core as a function of temperature at CMB pressure (136 GPa), based on the K_{Mg} from this study (red) and previous studies OS16 (O'Rourke & Stevenson, 2016) (blue), while other model parameters are identical. Model results from B16 (Badro et al., 2016) are also shown in gray for comparison. Blue, gray, and red arrows show the exsolution process with initially 2 wt % Mg, 1.6 wt %, 1.4 wt % Mg in the core, for OS16, B16, and this study, respectively. Note that Badro et al. (2016) also includes an initial period of cooling before exsolution begins.

Standard errors are shown in parentheses. Parameters b and c are found to be statistically insignificant after applying an F test (P value >0.05) (supporting information). Thus, K_{Mg} is better correlated with X_O compared to $1/T$ (Figure 1), suggesting a strong role for O in stabilizing Mg in Fe alloy and a lesser role for temperature. Similar behavior was found for many other elements, in particular, V, Cr, where O greatly enhances their core partitioning (Fischer et al., 2015; Siebert et al., 2013). We note that the $1/T$ term is related with enthalpy change of reaction (1), but a $1/T$ term is not required to explain the variations of K_{Mg} among different studies. Our finding contrasts with previous studies that found (Badro et al., 2016) or assumed (O'Rourke & Stevenson, 2016) that Mg partitioning strongly depends on temperature only (Figure S3a). Instead, the discrepancies among different studies can be largely explained by the variations of X_O (Figure 1b) (Badro et al., 2016; Chidester et al., 2017; Suer et al., 2017). The overall lower X_O in this study is probably due to higher carbon contents than those in previous studies (Badro et al., 2016; Suer et al., 2017), although carbon contents were not reported. Furthermore, this might be caused by the strong interactions between carbon and oxygen in the iron-rich liquid (Fischer et al., 2015).

The strong dependence of K_{Mg} on X_O (Figure 1b) indicates Mg exsolution is intimately connected to the oxygen content of the core during cooling. Moreover, X_O likely depends on T, P, and core composition (Figure S4), consistent with previous studies on oxygen partitioning in the core (e.g., Fischer et al., 2015, and references therein). Therefore, MgO exsolution indirectly depends on T, but it is drastically reduced due to the much weaker temperature dependence of K_{Mg} than previous studies (Badro et al., 2016; O'Rourke & Stevenson, 2016). To further explore the geophysical implications, we constructed an exsolution model for the Earth's core and couple it with a thermal model of the Earth, aiming to fully understand the effect of MgO exsolution on the Earth's thermal evolution. In the end, combined with paleomagnetic records, we offer potential observational tests for exsolution and inner core nucleation (ICN).

5. Geophysical Implications

We use the exchange coefficient, K_{Mg}, to calculate Mg solubility in the core during cooling (supporting information). Because of the uncertainties of temperatures, pressures, and core compositions in the core formation processes (Badro et al., 2016; O'Rourke & Stevenson, 2016), we treat the initial Mg content of the core as a free parameter and it ranges between 0 and 2 wt %. We adopt the model from O'Rourke and Stevenson (2016) for exsolution of an MgO-rich component: after Earth's core formation, initial concentrations of 0–2 wt % Mg, 3 wt % Si, and 6 wt % O are assumed to be well mixed and homogeneously dissolved in the core (O'Rourke & Stevenson, 2016). As the core cools, exsolution occurs within the core near the core mantle boundary (CMB) where the buoyant MgO-rich exsolution is instantaneously removed from the core.

Calculated Mg solubility in the core, assuming exsolution as a liquid, is shown in Figure 2, using K_{Mg} from this study and O'Rourke and Stevenson (2016), while keeping all other model parameters identical. Model results from Badro et al. (2016) are also shown as gray curve for comparisons (Figure 2). Calculated results (Figure 2) show a very weak temperature dependence of Mg solubility (change of Mg solubility ~0.3 wt % from 5000 K to 4000 K), much weaker than previous studies, for example, 1 wt % (Badro et al., 2016) and 3 wt % (O'Rourke & Stevenson, 2016). Importantly, this implies very limited exsolution of MgO out of the core during cooling. We also predict an MgO-rich exsolution, similar to previous studies (O'Rourke & Stevenson, 2016) in the range of 4000–5000 K (Figure S5).

To illustrate the exsolution process, we consider initially 1.4 wt % Mg (Figure 2). As the core cools, Mg content follows the red solid curve to the present-day value of ~1.1 wt %. In comparison, for results from OS16 (O'Rourke & Stevenson, 2016) with an initial 2 wt % Mg, the core is undersaturated in Mg; therefore,

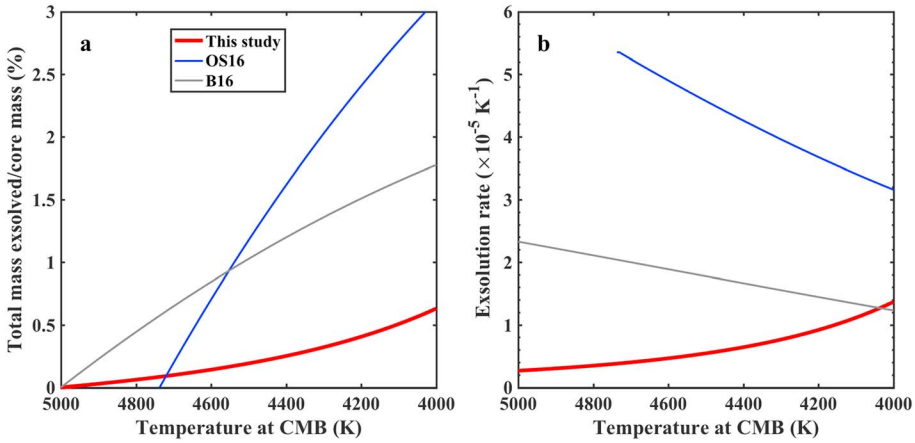

Figure 3. Calculated (a) total mass exsolved normalized to core mass and (b) exsolution rate as function of temperature at CMB pressure. Results assuming K_{Mg} from this study (red) and that from OS16 (O'Rourke & Stevenson, 2016) (blue) are shown, with other model parameters identical. Model results from B16 (Badro et al., 2016) are also shown in gray. For simplicity, inner core formation is not considered in this calculation but its effect is shown in Figure 4.

exsolution does not occur until ~4750 K. Subsequently, the Mg content drops along the blue dashed curve to ~0.7 wt % due to the strong temperature dependence. Similarly, the model results from B16 (Badro et al., 2016) are shown in the gray curve. This estimate of core Mg content at present day of ~1.1 wt % is an upper limit and could be further constrained by density and sound speed effects.

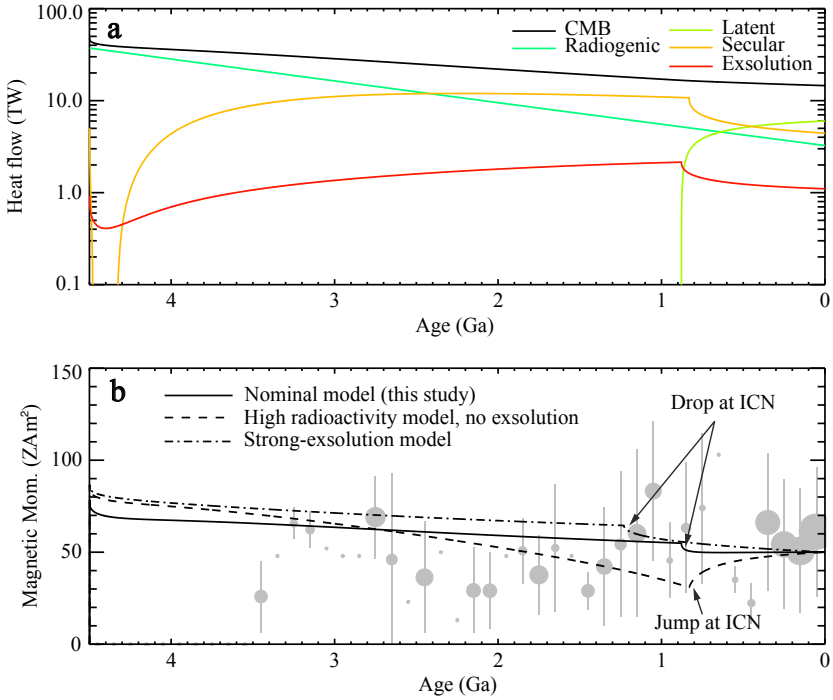

Figure 4. (a) Core heat flows in the "nominal" model with exsolution determined by this study and 3.2 TW of core radioactivity. (b) Rescaled magnetic moment throughout Earth's history for three models: (1) a "nominal" model with exsolution determined by this study and 3.2 TW of core radioactivity (black), (2) a "high radioactivity" model without exsolution but with 3.7 TW of core radioactivity (dashed), and (3) a strong-exsolution model with 9 times greater exsolution energy than this study and no core radioactivity (dash-dotted line). Virtual dipole moment (VDM) paleointensity data are from the Absolute Paleointensity (PINT) Database in Biggin et al. (2009) (circles). VDM data are the average within 100 Myr long bins with symbol size in logarithmic proportion to the number of data in each bin, error bars denote standard deviation of average within each bin, and bins with a single data point are shown as dots without error bars. More details on the nominal model are shown in Figure S6.

Following each Mg solubility curve in Figure 2, we calculate the total mass exsolved and exsolution rate as a function of temperature at CMB pressure (Figure 3). Our partitioning behavior produces a much lower exsolution rate than previously proposed (2×10^{-5} K^{-1}) (O'Rourke et al., 2017) to drive an early geodynamo (Figure 3b). We also note that exsolution rate increases as temperature decreases for this study in contrast to previous studies (Badro et al., 2016; O'Rourke & Stevenson, 2016), which is primarily due to the strong dependence of K_{Mg} on X_O. As the temperature decreases, X_O decreases and this in turn increases the exsolution rate.

To demonstrate the effect of exsolution on the thermal history of the core and the early geodynamo, we couple our predicted total (gravitation and reaction) MgO exsolution energy with a thermal model of the core (Driscoll & Bercovici, 2014) (supporting information). We compute three models (Figure 4b): (1) a "nominal" model with our experimental partitioning and 3.2 TW of core radioactivity (~400 ppm), as required to produce the present IC (inner core) size; (2) a "high radioactivity" model where no exsolution occurs, and 3.7 TW of core radioactivity is required; and (3) a "strong-exsolution" model with an exsolution rate 9 times the rate of the nominal model and no core radioactivity is needed. This latter model is similar to previous studies with strong exsolution either as MgO (Badro et al., 2016; O'Rourke & Stevenson, 2016) or SiO_2 (Hirose et al., 2017).

We note that such a large radioactive heat source (≥3.2 TW) is not favored for the core (e.g., Chidester et al., 2017; Corgne et al., 2007; Hirao et al., 2006) but is often assumed in order to match the empirical constraints (surface heat flow of 39 TW, upper mantle temperature of 1630 K, inner core radius 1221 km, and continuous dynamo) (e.g., Driscoll & Bercovici, 2014; Nimmo et al., 2004). To compare with paleomagnetic data (Biggin et al., 2015), we rescale the magnetic moment predicted by our models assuming present-day value ~50 ZAm^2 (Figure 4b).

The nominal model produces ~1 TW from exsolution (Figure 4a), which powers the dynamo but still requires unreasonably high radioactivity. The nominal model also predicts an IC age of ~850 Ma and a nearly constant magnetic moment history similar to the strong-exsolution model (Figure 4b) (O'Rourke et al., 2017). This is because in both cases exsolution dominates the buoyancy throughout Earth's history due to its high efficiency in generating buoyancy flux. Interestingly, both exsolution models produce drops in the magnetic moment following ICN (Figure 4b). These drops in magnetic moment are caused by a rapid decrease in the core secular cooling rate at ICN due to latent heat release at the ICB, which then results in a drop in exsolution rate and magnetic moment.

This is in contrast to a jump after ICN for the high radioactivity models (no exsolution) where compositional buoyancy driven by IC solidification dominates (Driscoll, 2016; Driscoll & Bercovici, 2014). Therefore, a drop in magnetic moment at ICN may offer an observational test for the exsolution. Additional high quality paleomagnetic data around 0.5–1 Ga would help to test this hypothesis (Biggin et al., 2009; Driscoll, 2016).

6. Conclusions

Based on our new interpretation of the Mg partitioning data, powering the early geodynamo requires a substantial alternative heat source. High core radioactivity would provide such a heat source but is unrealistic on the geochemical grounds (e.g., Chidester et al., 2017; Corgne et al., 2007; Hirao et al., 2006). The strong-exsolution model works if the core cooling rate is strongly coupled to its compositional evolution, particularly the change of oxygen content in the core. It has been suggested that oxygen in the core might be exhausted by SiO_2 exsolution (Hirose et al., 2017), and thus, MgO and SiO_2 exsolution may be coupled. In summary, we find that that MgO exsolution is unlikely to provide the power needed to drive the early geodynamo.

Acknowledgments

Data supporting Figure S1 are available in supporting information Table S1. We thank Emma Bullock for electron microprobe analysis, Suzy Vitale for FIB operations, and Victor Lugo for machining at Carnegie Institution of Washington. We also thank Sz-Chian Liou at University of Maryland and Fernando Camino at Brookhaven National Lab for help with FIB operations. We thank Timothy Strobel and Alexander Goncharov's generosity for sharing laser systems and other facilities. Special thanks for Jiachao Liu and Jie Li for donating a carbon standard and Stephen Elardo for synthesizing the basalt glass. We also thank Anat Shahar, Miki Nakajima, Renbiao Tao, Megan Duncan, and James Badro for discussions. We appreciate two anonymous reviewers for critical comments. Z. Du, C. Jackson, and N. Bennett thank the Carnegie Fellowship for financial support. The research is supported by NSF grant (EAR-1447311) to Y. Fei. Work at Yale University is supported in part by NSF grants (EAR-1321956 and EAR-1551348) to K. K. M. Lee. Portions of this work were performed at GeoSoilEnviroCARS (University of Chicago, Sector 13), Advanced Photon Source (APS), Argonne National Laboratory. GeoSoilEnviroCARS is supported by the National Science Foundation-Earth Sciences (EAR-1128799) and Department of Energy-GeoSciences (DE-FG02-94ER14466). This research used resources of the Advanced Photon Source, a U.S. Department of Energy (DOE) Office of Science User Facility operated for the DOE Office of Science by Argonne National Laboratory under contract DE-AC02-06CH11357.

References

Badro, J., Brodholt, P., Piet, H., Siebert, J., & Ryerson, F. J. (2015). Core formation and core composition from coupled geochemical and geophysical constraints. *Proceedings of the National Academy of Sciences of the United States of America*, *112*(40), 12,310–12,314. https://doi.org/10.1073/pnas.1505672112

Badro, J., Siebert, J., & Nimmo, F. (2016). An early geodynamo driven by exsolution of mantle components from Earth's core. *Nature*, *536*(7616), 326–328. https://doi.org/10.1038/nature18594

Biggin, A. J., Piispa, E. J., Pesonen, L. J., Holme, R., Paterson, G. A., Veikkolainen, T., & Tauxe, L. (2015). Palaeomagnetic field intensity variations suggest Mesoproterozoic inner-core nucleation. *Nature*, *526*(7572), 245–248. https://doi.org/10.1038/nature15523

Biggin, A. J., Strik, G., & Langereis, C. G. (2009). The intensity of the geomagnetic field in the late-Archaean: New measurements and an analysis of the updated IAGA palaeointensity database. *Earth, Planets and Space*, *61*(1), 9–22. https://doi.org/10.1186/BF03352881

Chidester, B. A., Rahman, Z., Righter, K., & Campbell, A. J. (2017). Metal-silicate partitioning of U: Implications for the heat budget of the core and evidence for reduced U in the mantle. *Geochimica et Cosmochimica Acta*, *199*, 1–12. https://doi.org/10.1016/j.gca.2016.11.035

Corgne, A., Keshav, S., Fei, Y., & McDonough, W. F. (2007). How much potassium is in the Earth's core? New insights from partitioning experiments. *Earth and Planetary Science Letters*, *256*(3-4), 567–576. https://doi.org/10.1016/j.epsl.2007.02.012

de Koker, N., Steinle-Neumann, G., & Vlcek, V. (2012). Electrical resistivity and thermal conductivity of liquid Fe alloys at high *P* and *T*, and heat flux in Earth's core. *Proceedings of the National Academy of Sciences of the United States of America*, *109*(11), 4070–4073. https://doi.org/10.1073/pnas.1111841109

Deng, J., Du, Z., Benedetti, L. R., & Lee, K. K. M. (2017). The influence of wavelength-dependent absorption and temperature gradients on temperature determination in laser-heated diamond-anvil cells. *Journal of Applied Physics*, *121*(2), 11.

Driscoll, P. E. (2016). Simulating 2 Ga of geodynamo history. *Geophysical Research Letters*, *43*, 5680–5687. https://doi.org/10.1002/2016GL068858

Driscoll, P. E., & Bercovici, D. (2014). On the thermal and magnetic histories of earth and Venus: Influences of melting, radioactivity, and conductivity. *Physics of the Earth and Planetary Interiors*, *236*, 36–51.

Fischer, R. A., Nakajima, Y., Campbell, A. J., Frost, D. J., Harries, D., Langenhorst, F., … Rubie, D. C. (2015). High pressure metal-silicate partitioning of Ni, Co, V, Cr, Si, and O. *Geochimica et Cosmochimica Acta*, *167*, 177–194. https://doi.org/10.1016/j.gca.2015.06.026

Hirao, N., Ohtani, E., Kondo, T., Endo, N., Kuba, T., Suzuki, T., & Kikegawa, T. (2006). Partitioning of potassium between iron and silicate at the core-mantle boundary. *Geophysical Research Letters*, *33*, L08303. https://doi.org/10.1029/2005GL025324

Hirose, K., Morard, G., Sinmyo, R., Umemoto, K., Hernlund, J., Helffrich, G., & Labrosse, S. (2017). Crystallization of silicon dioxide and compositional evolution of the Earth's core. *Nature*, *543*(7643), 99–102. https://doi.org/10.1038/nature21367

Huang, H., Fei, Y., Cai, L., Jing, F., Hu, X., Xie, H., … Gong, Z. (2011). Evidence for an oxygen-depleted liquid outer core of the Earth. *Nature*, *479*(7374), 513–516. https://doi.org/10.1038/nature10621

Konopkova, Z., McWilliams, R. S., Gomez-Perez, N., & Goncharov, A. F. (2016). Direct measurement of thermal conductivity in solid iron at planetary core conditions. *Nature*, *534*(7605), 99–101. https://doi.org/10.1038/nature18009

Ma, Z. (2001). Thermodynamic description for concentrated metallic solutions using interaction parameters. *Proceedings of Science Metallurgical and Materials Transactions B-Proceedings of Metallurgical Materials*, *32*(1), 87–103.

Nimmo, F., Price, G. D., Brodholt, J., & Gubbins, D. (2004). The influence of potassium on core and geodynamo evolution. *Geophysical Journal International*, *156*(2), 363–376. https://doi.org/10.1111/j.1365-246X.2003.02157.x

Ohta, K., Kuwayama, Y., Hirose, K., Shimizu, K., & Ohishi, Y. (2016). Experimental determination of the electrical resistivity of iron at Earth's core conditions. *Nature*, *534*(7605), 95–98. https://doi.org/10.1038/nature17957

Olson, P. (2013). The new core paradox. *Science*, *342*(6157), 431–432. https://doi.org/10.1126/science.1243477

O'Rourke, J. G., Korenaga, J., & Stevenson, D. J. (2017). Thermal evolution of Earth with magnesium precipitation in the core. *Earth and Planetary Science Letters*, *458*, 263–272. https://doi.org/10.1016/j.epsl.2016.10.057

O'Rourke, J. G., & Stevenson, D. J. (2016). Powering Earth's dynamo with magnesium precipitation from the core. *Nature*, *529*(7586), 387–389. https://doi.org/10.1038/nature16495

Pozzo, M., Davies, C., Gubbins, D., & Alfe, D. (2012). Thermal and electrical conductivity of iron at Earth's core conditions. *Nature*, *485*(7398), 355–358. https://doi.org/10.1038/nature11031

Rubie, D. C., Frost, D. J., Mann, U., Asahara, Y., Nimmo, F., Tsuno, K., … Palme, H. (2011). Heterogeneous accretion, composition and core-mantle differentiation of the Earth. *Earth and Planetary Science Letters*, *301*(1-2), 31–42. https://doi.org/10.1016/j.epsl.2010.11.030

Siebert, J., Badro, J., Antonangeli, D., & Ryerson, F. J. (2013). Terrestrial accretion under oxidizing conditions. *Science*, *339*(6124), 1194–1197. https://doi.org/10.1126/science.1227923

Suer, T.-A., Siebert, J., Remusat, L., Menguy, N., & Fiquet, G. (2017). A sulfur-poor terrestrial core inferred from metal–silicate partitioning experiments. *Earth and Planetary Science Letters*, *469*, 84–97. https://doi.org/10.1016/j.epsl.2017.04.016

Tarduno, J. A., Cottrell, R. D., Davis, W. J., Nimmo, F., & Bono, R. K. (2015). A Hadean to Paleoarchean geodynamo recorded by single zircon crystals. *Science*, *349*(6247), 521–524. https://doi.org/10.1126/science.aaa9114

Wade, J., & Wood, B. J. (2005). Core formation and the oxidation state of the Earth. *Earth and Planetary Science Letters*, *236*(1-2), 78–95. https://doi.org/10.1016/j.epsl.2005.05.017

Geophysical Research Letters

Supporting Information for

Insufficient energy from MgO exsolution to power early geodynamo

Zhixue Du[1], Colin Jackson[1,2], Neil Bennett[1], Peter Driscoll[3],
Jie Deng[4], Kanani K. M. Lee[4], Eran Greenberg[5], Vitali B. Prakapenka[5], Yingwei Fei[1]

[1] Geophysical Laboratory, Carnegie Institution of Washington, Washington, DC 20015, USA
[2] National Museum of Natural History, Smithsonian Institution, Washington, D.C. 20560, USA
[3]Department of Terrestrial Magnetism, Carnegie Institution of Washington, Washington DC 20015, USA
[4]Department of Geology and Geophysics, Yale University, New Haven, CT 06511, USA
[5]Center for Advanced Radiation Sources, University of Chicago, Chicago, IL 60637, USA

Contents of this file

Text S1
Figures S1 to S8
Tables S1 to S4

Introduction

This data set contains all the measurements of temperatures, pressure and elemental compositions of iron-silicate melting experiments. It also includes all the details of thermodynamic models of core exsolution, Earth's thermal models and dynamo model. Starting materials compositions are given in Table S1. Experimental conditions and compositions of recovered samples are listed in Table S2. Model parameters for exsolution model are shown in Table S3, as well as those for Earth's thermal model in Table S4. Figures are listed as Figs. S1-8, which describes in situ X-ray diffraction pattern (S1), ex-situ electron image (S2), compilation of Mg partitioning data (S3), compilation of oxygen and silicon partitioning data (S4), calculated composition of core exsolution (S5), Earth's thermal evolution from our model calculation (S6), calculated exsolution energy (S7) and elemental distribution of a recovery sample (S8).

Text S1

1.1 High-pressure experiments and elemental analysis

Three different starting materials are used in this study: pyrolite, basalt and (Mg,Fe)O ferropericlase. Synthesis procedures are as follows: the pyrolite glass is made by laser heated gas-levitation method above the liquidus temperature, under an oxygen fugacity approximately equal to the iron-wüstite (IW) buffer at 1 bar [*Gu et al.*, 2016]. Basalt glass synthesized at the IW buffer using a 1 atm furnace (1400 °C). Powder of $(Mg_{0.89},Fe_{0.11})O$ is synthesized following procedures from [*Du and Lee*, 2014]. The starting compositions are summarized in Table S2.

Starting materials are then ground with metal powders (pure Fe, FeSi or FeS) in an agate mortar for half an hour. Subsequently, silicate and metal powder mixture are loaded into pre-indented Re gasket and pressurized to 20-66 GPa using a diamond-anvil cell (DAC) with 300 or 350 μm culet size. Pyrolite glass is used as a pressure medium in all experiments on both sides of the sample chamber except experiment "15cc35B" where polycrystalline MgO is used. Pressures are measured by the first-order Raman shift of the diamond culet [*Akahama and Kawamura*, 2006] and confirmed by the equation state of iron[*Fei et al.*, 2016] by in-situ X-ray diffraction before heating. Pressures after melting are measured by first-order Raman shift of the diamond culet [*Akahama and Kawamura*, 2006] and we find they are within 10% of those before heating. Thermal pressures are estimated up to ~20% during heating and considered as uncertainties in pressure measurements (e.g., [*Du and Lee*, 2014]). Details of sample assembly can be found in Table S1, as well as loading procedures in previous study [*Du et al.*, 2015].

High-pressure melting experiments are conducted at GSECARS 13-ID-D beamline facility and peak temperatures are measured on both sides simultaneously[*Prakapenka et al.*, 2008]. Melting is identified by the appearances of diffuse X-ray diffraction (Fig. S1) and confirmed by quench textures from recovered samples (Fig. S2). One exception is experiment "15cc35B" which was conducted in the Department of Geology and Geophysics at Yale University. This sample was ramp-heated and held at the highest temperature for 1 second before it quenched to room temperature [*Du and Lee*, 2014]. Temperatures are found to be within mutual uncertainties of each side, except for experiment "16cc48M2." For this experiment, the higher temperature side is taken because the lower temperature was likely biased due to a slight misalignment of the temperature measurement with center of the hotspot (likely caused by asymmetric coupling between laser and sample material) or a the thick absorption layer between the diamond anvil and melt spot [*Deng et al.*, 2017].

All recovered samples are extracted from the rhenium gasket using a laser cutter, and glued with epoxy onto a copper grid. This procedure is similar with that described previously in [*Du and Lee*, 2014]. The cross section of melt spots are exposed and polished at 30 kV, 600 pA by Ga ions using focus ion beam (AURIGA, Zeiss Instruments) located at Carnegie Institution of Washington (CIW). Chemical analyses are conducted using an electron microprobe (JEOL 8530F) with a 10 kV and 5-10 nA, 1μm diameter beam at CIW. Standards used for each element are list as follows: ENAL ($MgSiO_3$ glass with 5.0 wt% Al_2O_3) for Mg, Al, Si; Basalt glass (basalt812) for Ca;

magnetite (Fe_3O_4) for Fe, O; Pure Fe (NIST2168) for Fe; Pure Re metal for Re; NiS or FeS_2 for S; synthetic Fe_7C_3 for C [*Liu et al.*, 2016]. Backgrounds for all elements are measured on pure Fe (NIST2168). In particular, backgrounds for C and O are found to be 0.4±0.1 wt.% and 0.3±0.1 wt.% respectively. For carbon analysis in the metals, identical procedures are used as previous study [*Deng et al.*, 2013; *Smith et al.*, 2016]. Results are summarized in Table S1, with backgrounds subtracted.

1.2 Parameterization of K_{Mg}

Following the previous approach [*Ma*, 2001] and considering the low concentration of Mg (X_{Mg} <0.01), we neglect the self-interaction term and high-order terms and therefore K_{Mg} can be parameterized as follows:

$$\log_{10}(K_{Mg}) = a + b/T + cP/T + d\log_{10}(1-X_O) + e\log_{10}(1-X_C) + f\log_{10}(1-X_S)$$

Where *T is* temperature in kelvin and *P* is pressure in GPa, X_O, X_C, X_S are the mole fraction of oxygen (O), carbon(C) and sulfur (S) in the iron-rich liquid respectively. Parameters *a*, *b*, *c*, *d*, *e* and *f* are determined using a weighted linear least-squares fit with the following dataset, weighted by the uncertainties of X_O. We note that interaction parameters *d, e, f* are assumed to be a constant, while some previous studies assume they are inversely proportional to temperature (e.g., [*Wade and Wood*, 2005]).We find *d* is the only significant parameter, while *b*, *c*, *e*, *f* are statistically insignificant after applying *F*-test (P value > 0.05). We obtain

$$\log_{10}(K_{Mg}) = -3.9(0.2) - 18.6(2)\log_{10}(1-X_O)$$

with R^2=0.7 and standard errors are shown in parentheses. See Fig. S1b for fitted results. In addition, we also provide the fitting results assuming all parameters are significant in Table S3.

Selection of dataset:

All data from this study and B16 [*Badro et al.*, 2016] are included, as well as some results from C17[*Chidester et al.*, 2017] (Run #B49 and #B66) and S17 [*Suer et al.*, 2017] (Run #6, #7 and #9). Those experimental runs from S17[*Suer et al.*, 2017] are not included for the reasons below: Run #1 and #3 are previously reported in B16; The totals in Run #2 are 114% for silicate and 88% for metal, therefore we consider the results are potentially erroneous. Reported X_O in Run #42, #50, #56 from C17 [*Chidester et al.*, 2017] are not direct measurements, instead, calculated based on previous results[*Fischer et al.*, 2015], likely with large uncertainties, thus are not included in our dataset for regression.

Our results (Fig. 1b) show Mg partitioning strongly correlates with oxygen in the liquid iron, suggesting a potentially pivotal role of oxygen controlling Mg partitioning. Due to the large variations of uncertainties reported for X_O, e.g., the error bars from S17 [*Suer et al.*, 2017] are significantly larger than the rest of the dataset. Therefore, we use least-squares fit weighted by the uncertainties of X_O.

Those included in the dataset are shown in filled symbols and those not included are shown with open symbols (Fig. S3). It is worth noting, samples (some runs in C17[*Chidester et al.*, 2017]), although with potentially large uncertainties, are still consistent with other datasets for the overall trend (Fig. S1b, S3b).

1.3 Exsolution of MgO out of Earth's core

After Earth's core formed, we assume an initial composition of 0-2 wt% Mg, 3 wt % Si, 6 wt% O and all the elements are well mixed in the core. We note that Mg might not be well mixed in the core [*Landeau et al.*, 2016], however, the well-mixed case provides an upper limit to the power generated by exsolution [*Badro et al.*, 2016]. We adopt the model for exsolution of an MgO-rich component during core cooling [*O'Rourke and Stevenson*, 2016]. Given the increasing O partitioning with pressure (pressure dependence, c_O is positive, Table S3) and zero pressure dependence of Mg and Si, exsolution always occurs at lowest pressure and temperature within the core near core mantle boundary. Also note that estimates of oxygen content in the core range from 0.5 to 5 wt% in the Earth's core (e.g., [*Badro et al.*, 2015; *Fischer et al.*, 2015; *Huang et al.*, 2011; *Rubie et al.*, 2011; *Wade and Wood*, 2005]), lower than the assumed 6 wt% in this study (Fig. 1b). Therefore 6 wt% of O in the core would serve as an upper limit for the exsolution energy.

Here we consider the core cools from 5000K to 4000K. At every cooling step (1K), the mass of exsolution is calculated by solving reactions 1-3 as followed and equations of mass balance (see supplements of [*Rubie et al.*, 2011]). If the mass of exsolution is negative or zero, it means the core is undersaturated with mantle components, no exsolution is expected. If the mass of exsolution is positive, then exsolution is instantaneously removed from the core [*O'Rourke and Stevenson*, 2016].

Exsolution as a liquid

In addition to reaction (1), two reactions are considered:

$$SiO_2^{\text{silicate melt}} + 2Fe^{\text{metal}} \leftrightharpoons 2FeO^{\text{silicate melt}} + Si^{\text{metal}} \quad (2)$$

$$FeO^{\text{silicate melt}} \leftrightharpoons Fe^{\text{metal}} + O^{\text{metal}} \quad (3)$$

Exchange coefficients are $K_{Si}=X_{Si}/X_{SiO_2}/(X_{Fe}/X_{FeO})^2$ and $K_O=X_{Fe}X_O/X_{FeO}$, where X_{FeO}, X_{SiO_2}, X_{Fe}, X_{Si}, X_O are the mole fraction of FeO and SiO_2 component in silicate melt and Fe, Si, O component in iron-rich liquid metal respectively. Both K_{Si} and K_O are experimentally determined and parameterized in a similar way as for reaction (1), which are taken from [*Fischer et al.*, 2015] and listed in Table S3.

Exsolution energy:

Total exsolution energy E_x consists of two parts: gravitational energy and reaction energy, *i.e.*,

$$E_x = \Delta E_{grav} + E_{re} \quad (4)$$

Gravitational energy release (ΔE_{grav}) upon exsolution is estimated by calculating the difference of total energy difference before and after exsolution.

Total gravitational energy is given by:

$$E_{grav} = -\int_0^{R_\oplus} \frac{GM(r)}{r} 4\pi r^2 \rho(r) \mathrm{d}r \quad (5)$$

where, G is the gravitational constant, $M(r)$ is the mass of the core within the radius r, $\rho(r)$ is the density of the core at radius r and $R_\oplus$ is the radius of the core. In addition, compositional expansivity $\alpha_x = -1/\rho(\partial\rho/\partial x) \approx 1.12$, where x is the concentration (in

weight) of the light elements, i.e., Mg, O and Si that exsolve out of the core[*O'Rourke and Stevenson*, 2016].

Reaction energy (E_{re}) is calculated by sum of enthalpy change for reaction 1-3

$$E_{re} = \sum_i m_i \Delta H_i \quad (6)$$

Where, i are exsolved components: MgO, SiO_2, FeO; m_i is molar number of exsolution. ΔH_i is enthalpy change of reaction 1-3 involving exsolving component i.

For reaction (1), $\Delta H_{Mg} = \Delta H_{f,FeO} - \Delta H_{f,MgO}$, where $\Delta H_{f,FeO}$ and $\Delta H_{f,MgO}$ are the enthalpy of formation for FeO and MgO respectively, which are taken as −630 kJ/mol and –253 kJ/mol at 1-bar and 3100K from [*Barin*, 1995]. Similarly for reaction (2), $\Delta H_{Si} = 2\Delta H_{f,FeO} - \Delta H_{f,SiO2}$, where $\Delta H_{f,SiO2}$ is the enthalpy of formation for liquid SiO_2, which is −915 kJ/mol at 1-bar and 3100 K from [*Barin*, 1995]. Lastly, for reaction (3), $\Delta H_O = -\Delta H_{f,FeO}$. In this study, to the first order approximation, we assume ΔH_{Mg}, ΔH_{Si}, ΔH_O are constants, *i.e.,* which are pressure and temperature insensitive. We note that *1/T* term for reaction (1) is related with ΔH_{Mg} but it may not be identical. Therefore *1/T* term being statistically insignificantly (b=0) is not necessarily in contradictory with non-zero ΔH_{Mg}.

1.4 Thermal model of Earth's core

Core

The secular cooling of the core is

$$\dot{T}_c = \frac{Q_{rad,c} - Q_{cmb}}{M_c c_c + C_{ic} + C_x} \quad (7)$$

where T_c is the average core temperature, $Q_{rad,c}$ is core radiogenic heat flow, Q_{cmb} is CMB heat flow, M_c is core mass, c_c is core specific heat, and C_{ic} and C_x are energy released from inner core growth and exsolution per kelvin. The core adiabatic and liquidus temperature profiles are approximated as quadratic.

The core adiabatic and liquidus temperature profiles are

$$T_{ad} = T_{cmb} + T_{ad1}(R_c^2 - r^2) \quad (8)$$

$$T_{liq} = T_{liq1} + T_{liq2}(R_c^2 - r^2) \quad (9)$$

The intersection of $T_{ad} = T_{liq}$ occurs at the inner core boundary (ICB),

$$R_{icb} = \sqrt{R_c^2 + \frac{T_{liq1} - T_{cmb}}{T_{liq2} - T_{ad1}}} \quad (10)$$

Energy released at the ICB is

$$Q_{ic} = C_{ic}\dot{T}_c \quad (11)$$

where the energy released at the ICB per temperature drop is

$$C_{ic} = A_{ic}\,\rho_{ic}(L_{ic} + E_{ic})\frac{dR_{ic}}{dT} \quad (12)$$

and

$$\frac{dR_{ic}}{dT} = \frac{1}{2R_{ic}(T_{ad1} - T_{liq1})} \quad (13)$$

Given the preferred MgO partitioning behavior above we add MgO exsolution from the core to the thermal and buoyancy budget of the core to a simple thermal history model of the Earth. The total (gravitational + reaction) energy released by exsolution per kelvin is parameterized as:

$$C_x = \alpha_0 + \alpha_1 T_{cmb} + \alpha_2 T_{cmb}^2 + \alpha_3 T_{cmb}^3 \quad (14)$$

where the coefficients α_0 , α_1 , α_2 , α_3 are derived from Fig. S7 and listed in Table S4. The exsolution power is then

$$Q_x = -C_x \dot{T}_c \tag{15}$$

and exsolution is assumed to occur throughout the Earth's history, *i.e.,* in this study, from T=5000 K to present day at 4000K.

Dynamo

The magnetic dipole moment $\mathcal{M}$ is estimated from the empirical scaling law,

$$\mathcal{M} = 4\pi R_c^3 \gamma_d \sqrt{\rho/2\mu_0}(F_c D_c)^{1/3} \tag{16}$$

where γ_d= 0.2 is the saturation constant for fast rotating dipolar dynamos, μ_0=4π ×10^{-7} H m^{-1} is the magnetic permeability of the vacuum, $D_c = R_c - R_{ic}$ is the dynamo region shell thickness, R_c and R_{ic} are outer and inner core radii, respectively, and F_c is the core buoyancy flux [*Olson and Christensen*, 2006]. The total core buoyancy flux F_c is the sum of the thermal, compositional and exsolution buoyancy fluxes,

$$F_c = F_{th} + F_\chi + F_x \tag{17}$$

where the buoyancy fluxes are

$$F_{th} = \frac{\alpha_c g_c}{\rho_c c_c} q_{c,conv} \tag{18}$$

$$F_\chi = g_i \frac{\Delta\rho_\chi}{\rho_c} \left(\frac{R_{ic}}{R_c}\right)^2 \dot{R}_{ic} \tag{19}$$

$$F_x = g_c \frac{\Delta\rho_x}{\rho_c} u_x \tag{20}$$

where the subscript c refers to bulk core properties, core convective heat flux is $q_{c,conv} = q_{cmb} - q_{c,ad}$, gravity at the ICB is approximated by $g_{ic} = g_c R_{ic}/R_c$, and the outer core compositional density difference is $\Delta\rho_\chi = \rho_c - \rho_\chi$ with ρ_χ the light element density. $\Delta\rho_x = \rho_c - \rho_x$ is the density difference between the bulk core and the exsolution.

The exsolution buoyancy flux F_x is driven by the excess density of residual iron following MgO exsolution to the top of the core. This residual iron-rich fluid is both denser and hotter (due to gravitational energy release + heat of reaction) than the ambient core fluid. However, the density increase is larger than that associated with the heating so that residual iron-rich fluid sinks back in to the outer core. The exsolution velocity u_x is:

$$u_x = \dot{M}_x/\rho_x A_c \tag{21}$$

where ρ_x is the density of the exsolution, A_c is the CMB area, and the exsolution mass rate is

$$\dot{M}_x = \frac{dM_x}{dT}\dot{T}_c \tag{22}$$

The mass exsolved per temperature drop $\frac{dM_x}{dT} = f_x C_x$, $f_x \approx 6.1\times10^{-8}$ kg/J. where f_x is the conversion factor from exsolved mass to total exsolution energy. This can also be derived from Fig. 3b similarly as for C_x.

The isentropic core heat flux at the CMB, proportional to the gradient of (15) is

$$q_{c,ad} = 2k_c R_c T_{ad1} , \tag{23}$$

Where core thermal conductivity is approximated by the Wiedemann-Franz law,

$$k_c = \sigma_c L_c T_{cmb} , \tag{24}$$

and electrical conductivity is σ_c and L_c is the Lorentz number. For typical values of high pressure-temperature iron (e.g, [*de Koker et al.*, 2012; *Pozzo et al.*, 2012]), $\sigma_c = 10 \times 10^5$ Ω^{-1} m^{-1} and $L_c = 10 \times 10^5$ $W\Omega\,K^{-1}$.

Mantle

The thermal evolution of the mantle is the same as in [*Driscoll and Bercovici*, 2014] except that there is no heat lost by melt eruption (i.e. $\epsilon_{erupt} = 0$) and radiogenic decay is now the sum of the four major decaying species: ^{238}U, ^{235}U, ^{232}Th and ^{40}K. The decay of each species produces radiogenic heat of

$$Q_{rad,i}(t) = Q^*_{rad,i} exp((t^* - t)/\tau_i) \quad (25)$$

Where *i* refers to each species listed in Table S4 and t^* = 4.5 Gyr.

1.5 Attainment of equilibrium

Under our experimental conditions, silicate and Fe alloy are coexisting in the liquid state. Atomic diffusivity in our experiments are estimated > 10^{-9} m^2/s [*Karki et al.*, 2013] for the silicate melt [*Adjaoud et al.*, 2011; *Karki*, 2010] and Fe liquid[*Posner et al.*, 2017]. For 10 seconds of heating while the samples are molten at the peak temperature, the diffusion length scale is ~100 μm which is much greater than our melt spot (~20 um). Therefore, equilibrium can be reached. This is further validated by uniform distribution of elemental distributions in our quenched Fe alloy and silicate melt. In Fig. S8, it is shown as an example, Mg content in the iron alloy, as well as MgO content in silicate melt, varies by less than 10% relative standard deviation across each region.

1.6 Effect of secondary fluorescence

Special care is taken to identify any possible effect of secondary fluorescence[*J Wade and Wood*, 2012]. For experiment "16cc33C" at 3000K, the measured Mg content is below the detection limit (40±10 ppm). In this experiment the Fe alloy phase is at least 2 by 5 μm in size, thus for a metal of this size, the effect of secondary fluorescence is negligible. In all other experiments the Mg content in the alloy is well above the detection limit and the Fe alloy phase is similar in size or bigger than that in "16cc33C". Additional evidence comes from the uniform distribution of Mg in Fe metal, which indicates secondary fluorescence effect is minimal (Fig. S8). Therefore we conclude, our measurements of Mg in Fe metal are not compromised by secondary fluorescence[*J Wade and Wood*, 2012].

1.7 Speciation of Mg in the iron-rich liquid

The underlying assumption of MgO dissolution by reaction (1) is that MgO is dissolved in the iron-rich metal as Mg, which is adopted in previous studies[*Badro et al.*, 2016; *O'Rourke and Stevenson*, 2016; *Wahl and Militzer*, 2015]. This assumption is supported by high-pressure experiments that demonstrate Mg species can be dissolved in iron liquid when equilibrated with molten Mg metal[*Dubrovinskaia et al.*, 2005].

It is worth noting that Mg might also be dissolved in iron-rich liquid as MgO. In this case, Mg is not a neutrally charged atom, instead, Mg is bonded with O atom and this "MgO" species is mixed in iron-rich liquid. Therefore, the reaction should be written as:

$$MgO^{\text{silicate melt}} = MgO^{\text{metal}} \quad (26)$$

Then, the reaction can defined as $K^* = X_{MgO}^{metal}/X_{MgO}^{silicate\ melt}$, where X_{MgO}^{metal}, $X_{MgO}^{silicate\ melt}$ are the mole fractions of the MgO components in the iron-rich liquid and silicate melt respectively. Similar to reaction (1), K^* can be parameterized as:

$$\log_{10}(K^*) = a + b/T + cP/T + d\log_{10}(1-X_O) + e\log_{10}(1-X_C) + f\log_{10}(1-X_S)$$

Considering our selected dataset, we found none of parameters are statistically significant, i.e., $R^2=0$, in contrast to $R^2=0.7$ by considering reaction (1). Therefore we conclude K_{Mg}, not K^*, describes the dominant dissolution reaction for Mg.

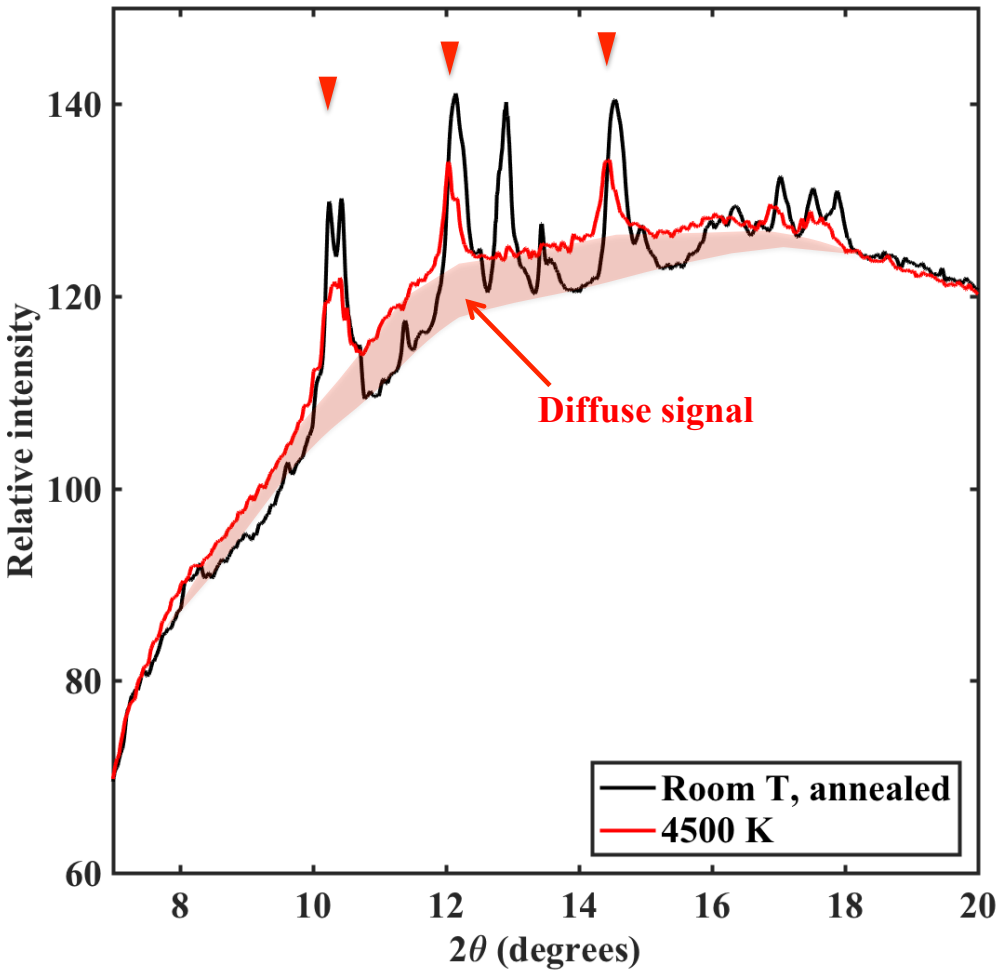

Fig. S1. *In situ* X-ray diffraction patterns taken at 66 GPa, room temperature after annealing (black) and peak temperature 4500K (red). Diffuse signal is shown in shaded area, indicating melting of sample (e.g., [*Anzellini et al*., 2013; *Fiquet et al*., 2010]). Downward triangles denote the (Mg, Fe)O peaks, mostly from liquidus phase shown in Fig. S2. Other peaks from both patterns can be interpreted as starting material (iron-sulfur alloy and annealed pyrolite glass).

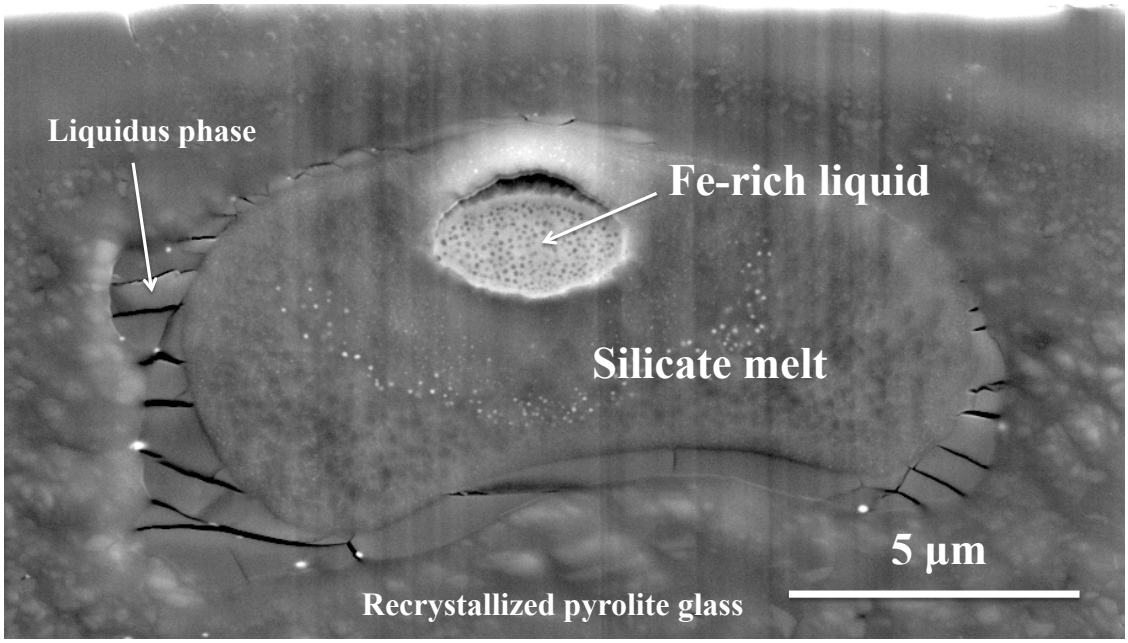

Fig. S2. Cross section of a recovered sample from 66 GPa, 4500K, from the experiment "16cc48M2". Iron-rich metal and surrounding silicate shows semi-spherical shapes, confirming melting of the sample at the peak temperature before quenching. Silicate melt is rimmed by liquidus phase (Mg,Fe)O, which is then surrounded by recrystallized pyrolite glass (composed primarily of bridgmanite and ferropericlase phases). The sharp boundary between liquidus phase and surrounding silicate is due to their distinct compositions and textures. Heating lasers from both sides are directed from the top and bottom in this figure. It should be noted that bright spots (0.1-0.2 um iron rich blebs), about half-way between the Fe-rich liquid and liquidus phase, are avoided during elemental analysis. We consider these blebs are probably un-coalesced Fe-rich liquid at peak PT conditions, which might compromise our analysis for silicate melt. The brightness of the material above "Fe-rich" liquid is most likely due to charging, as there is a decompression gap between the silicate melt and Fe-rich liquid.

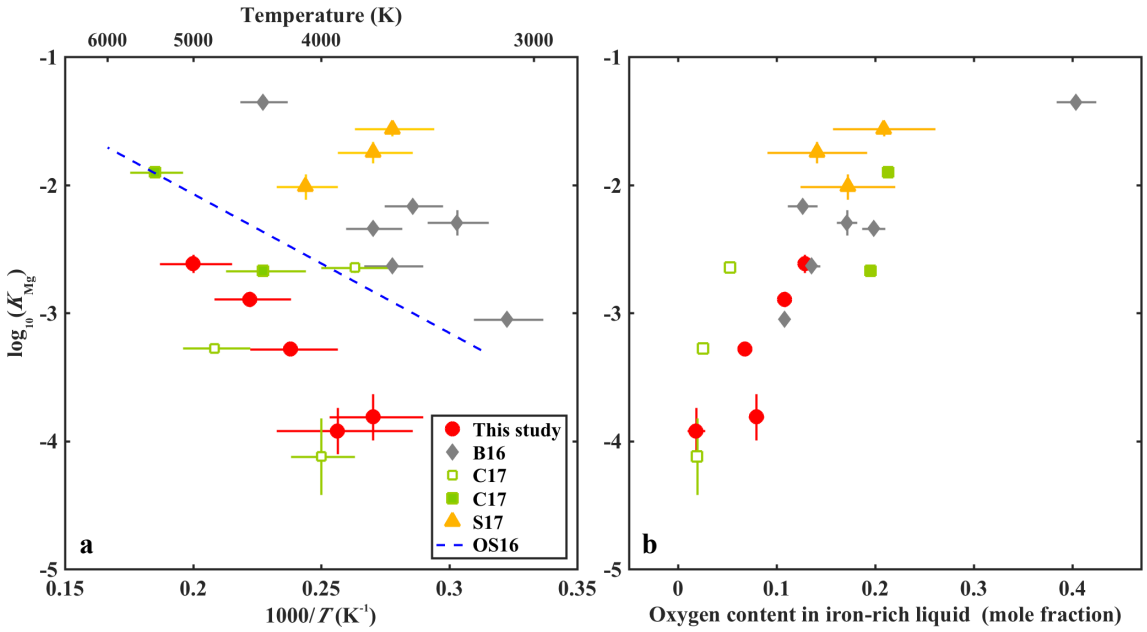

Fig. S3. Exchange coefficient (K_{Mg}) as a function of reciprocal temperature (1000/T) (a) and oxygen content in iron-rich liquid (b) in red circle (this study), gray triangle (B16 [*Badro et al.*, 2016]), green square (C17 [*Chidester et al.*, 2017]) and yellow triangle (S17 [*Suer et al.*, 2017]). Assumed values are plotted as blue dashed line (OS16 [*O'Rourke and Stevenson*, 2016]). Experimental data for this study are from Table S1. The error bar corresponds to 1σ uncertainties. Data included for the dataset are shown in filled symbols while those not included in open symbols (See text in Supporting Information).

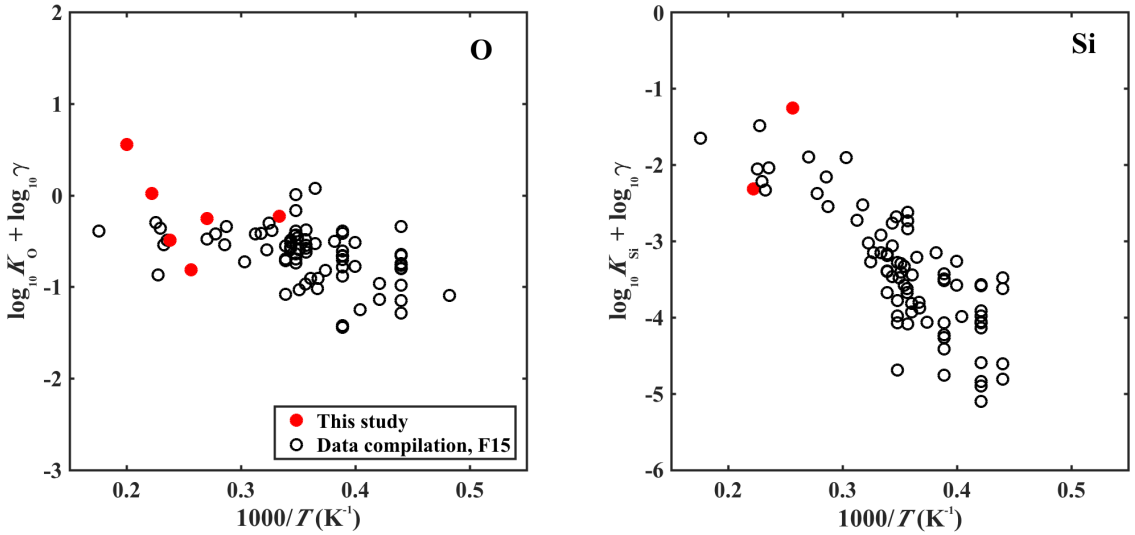

Fig. S4. Exchange coefficients for oxygen (K_O) and silicon (K_{Si}) as a function of reciprocal temperature (1000/T), corrected for activity of iron-rich liquid, for this study in red solid circles and previous studies in open circles taken from F15 [*Fischer et al.*, 2015]. Note that the data from this study are in good agreement with data complied in [*Fischer et al.*, 2015]. K_O and K_{Si} are defined after reaction (2) and (3) respectively in Supporting Information. And activity coefficient γ is calculated at given composition of iron-rich liquid, following the previous approach [*Ma*, 2001; *Wade and Wood*, 2005]. Interaction parameters $\varepsilon_{Si}^{Si} = 12.4$, $\varepsilon_C^{Si} = 9.7$, $\varepsilon_S^{Si} = 8.9$ [*Steelmaking*, 1988], $\varepsilon_O^{Si} = -5$ $\varepsilon_O^O = -1$ [*Tsuno et al.*, 2013], $\varepsilon_S^O = 0$ [*Tsuno et al.*, 2011], $\varepsilon_C^O = 8$ [*Fischer et al.*, 2015] are taken at reference temperature 1873 K. Note that only two data points are shown for K_{Si} due to either no Si is added to the starting material or Si is below detection limit in those experiments.

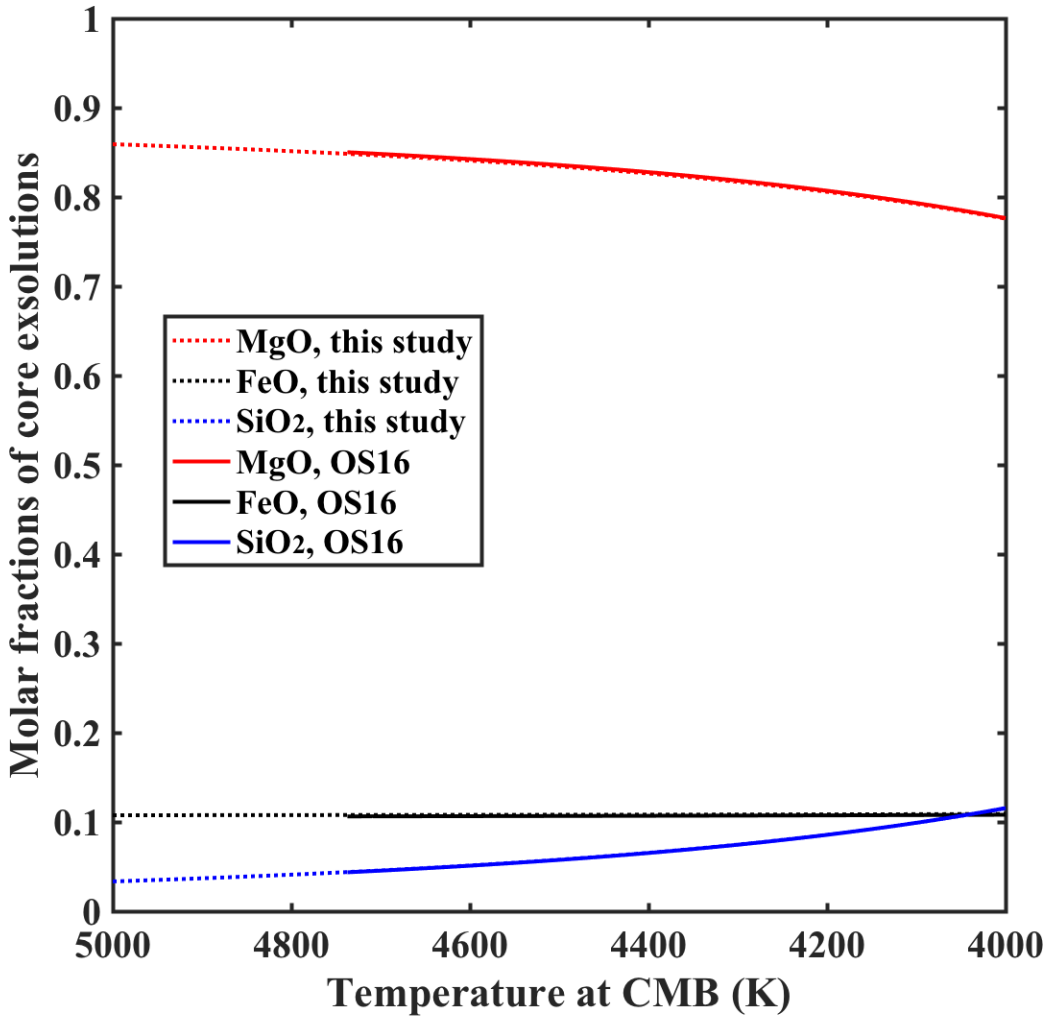

Fig. S5. Calculated compositions of core exsolutions as a function of temperature at CMB for this study (dotted lines) and for OS16 [*O'Rourke and Stevenson*, 2016] (dashed lines), assuming exsolutions as a liquid. MgO, FeO and SiO_2 components are shown in red, black and blue respectively. Only the MgO component is calculated in the model for B16 [*Badro et al.*, 2016] and therefore is not shown here. Note that for OS16 [*O'Rourke and Stevenson*, 2016], exsolutions do not occur until ~4750K, which corresponds to the case shown in Fig. 2.

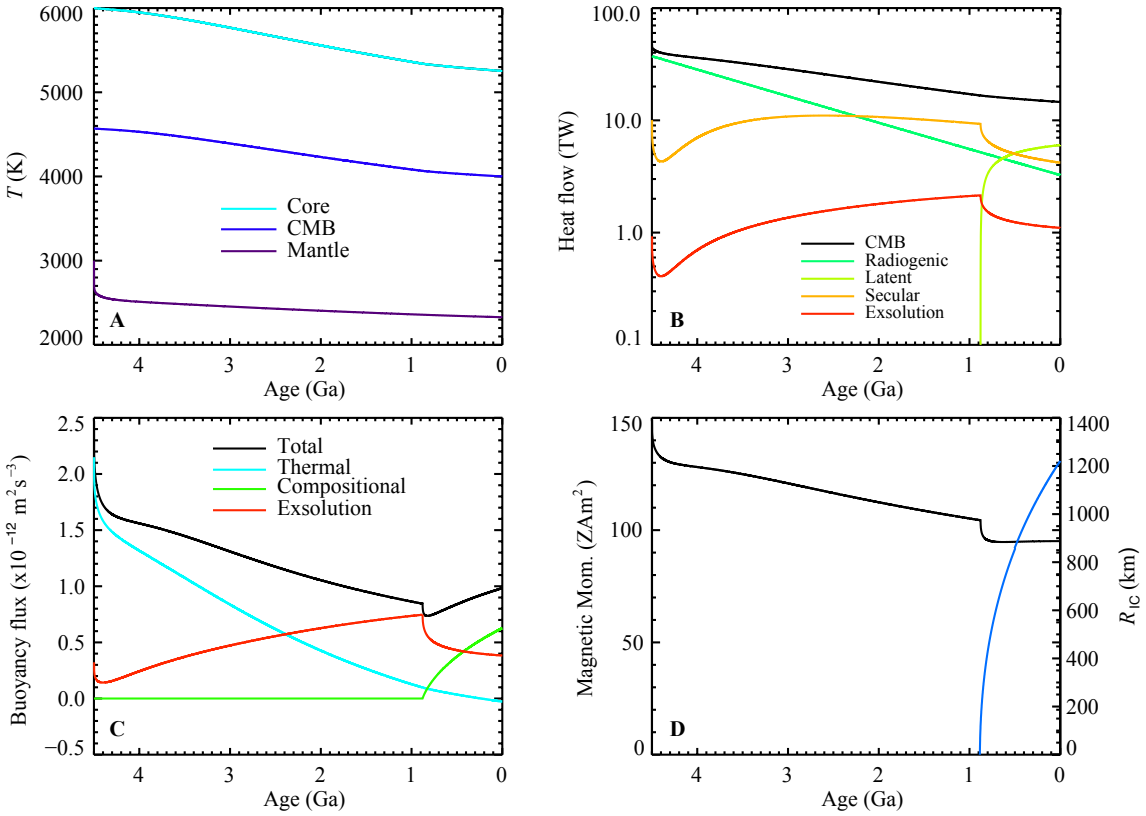

Fig. S6. Thermal history model including MgO exsolution determined by this study. 3.2 TW of ^{40}K in the present-day core is needed to produce temperatures, heat flows, and inner core radius consistent with observations. (a) Average core (cyan), CMB (blue), and average mantle temperatures (purple). (b) Core heat flows. (c) Core buoyancy fluxes. (d) Magnetic moment (black) and inner core radius (blue).

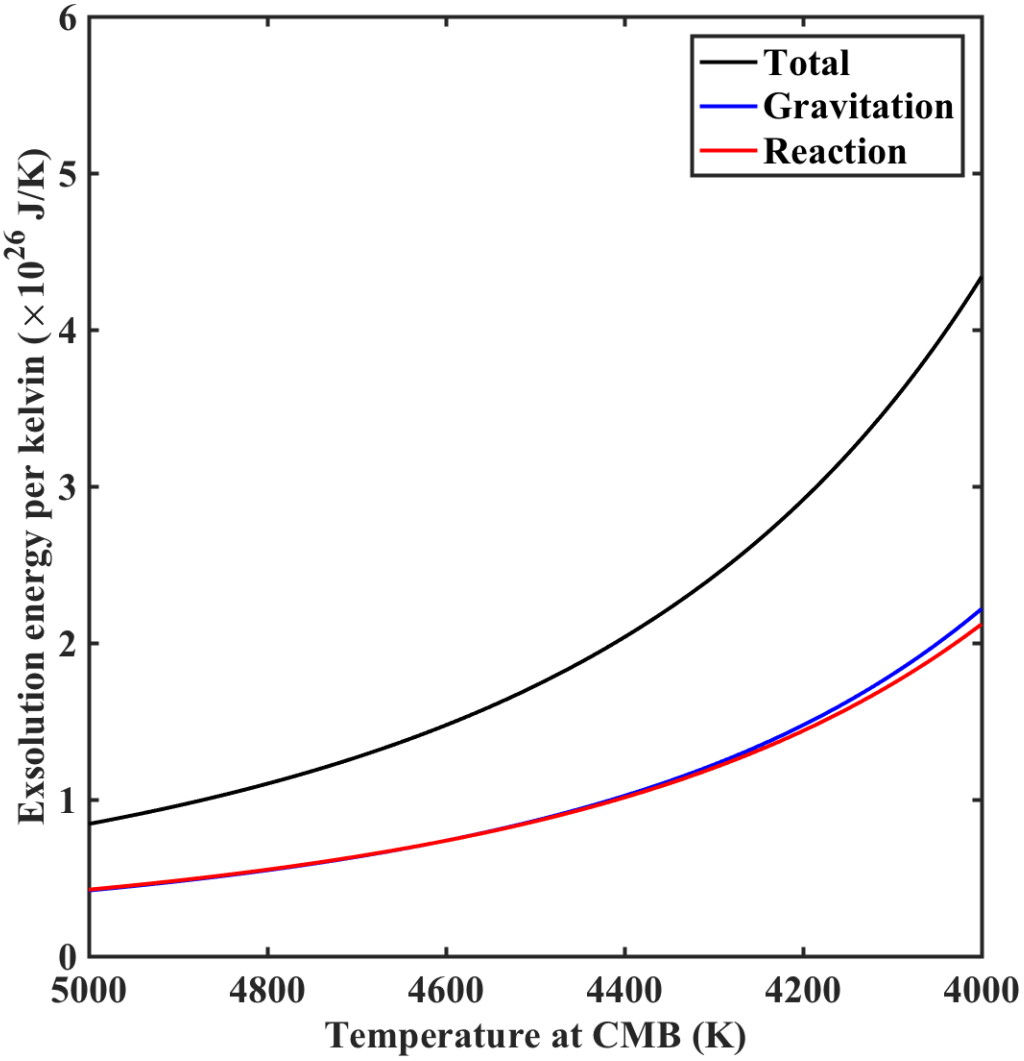

Fig. S7. Calculated exsolution energy as a function of temperature at CMB for this study. Total, gravitation and reaction exsolution energies are shown in black, blue and red curves, respectively.

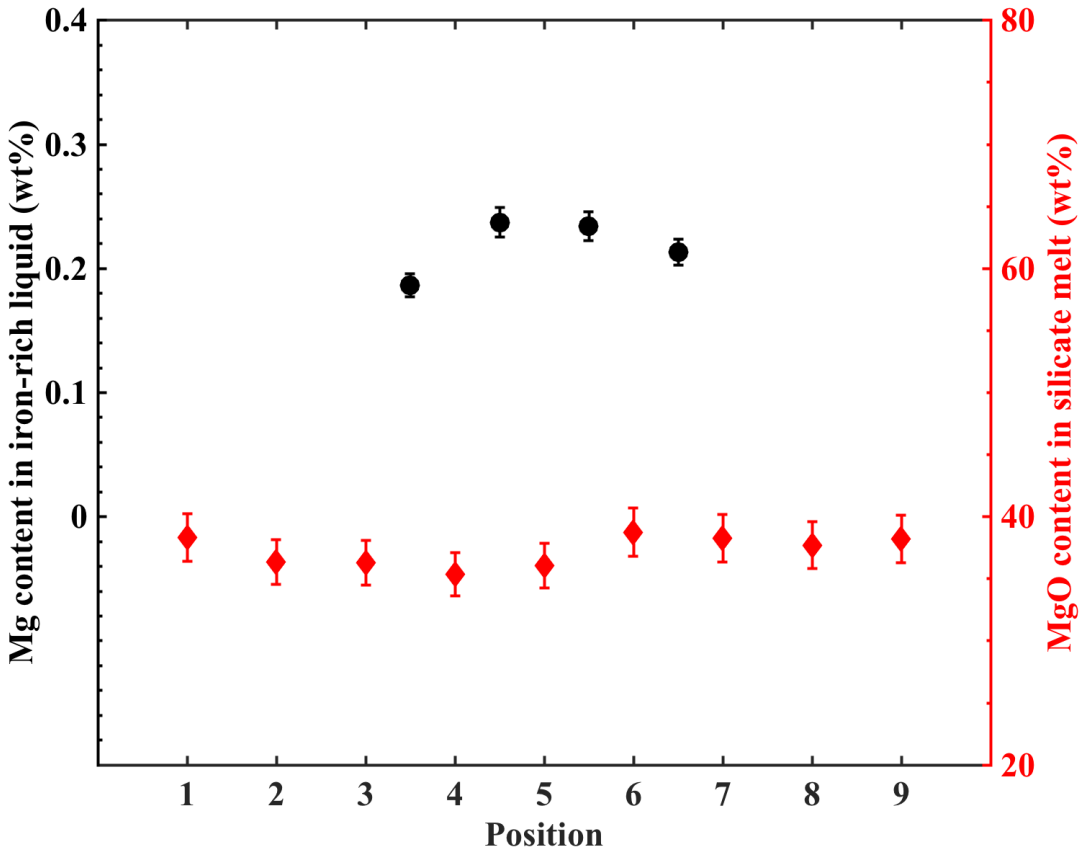

Fig. S8. Mg distribution in Fe metal (black circles, left axis) and MgO content distribution in silicate melt (red diamonds, right axis). The uniform elemental distribution (relative standard deviation < 10%) indicates attainment of equilibrium in our experiments, as well as negligible effect from secondary fluorescence (text in Supporting Information). We note that there is a texture in the quenched iron-rich liquid at the scale of ~ 0.1 μm, which is much smaller than the electron beam size (~1 μm). Therefore we consider each analysis (3-5 spots in the metal) are representative of the average composition of the quenched metal and confirm that they are uniform with each other to within 10% relative standard deviation (Fig. S8).

Experimental No.	16cc48M2		16cc48A		16cc48C		17cc33B		15cc35B		16cc33C	
Starting material	(Fe,S), pyrolite		(Fe,S), pyrolite		(Fe,S), pyrolite		FeSi, basalt		Fe, (Mg,Fe)O		(Fe,S), pyrolite	
Pressure medium	pyrolite		pyrolite		pyrolite		pyrolite		MgO		pyrolite	
Pressure (GPa)	66 (6)		44 (4)		44 (4)		33 (3)		40 (3)		22 (2)	
Temperature (K)	4500 (300)		3700 (250)		4200 (300)		3900 (300)		5000(350)		3000 (200)	
Metal	wt%	σ	wt%	σ	wt%	σ	wt%	σ	wt%	σ	wt%	σ
Fe	79.13	0.69	67.64	0.74	67.43	0.73	67.18	1.05	78.23	2.96	83.18	0.48
Mg	0.22	0.03	0.012	0.01	0.046	0.01	0.05	0.03	1.60	0.29	<0.004	-
O	4.34	0.19	2.91	0.29	2.55	0.22	0.72	0.41	6.16	0.28	1.52	0.32
Si	0.96	0.07	-	-	-	-	27.56	0.48	-	-	-	-
S	5.32	0.10	14.02	0.82	22.47	0.84	-	-			6.58	0.09
C	7.26	0.30	5.62	1.80	3.45	0.86	2.76	0.63	13.68	3.21	7.09	0.26
Re	1.39	0.08	10.06	0.41	3.32	0.86	-	-	-	-	-	-
others*	-	-	-	-	-	-	1.65	0.10	-	-	-	-
Total	98.68	0.48	100.32	0.74	99.27	0.17	100.07	0.87	99.68	0.95	98.37	0.95
Silicate melt												
MgO	38.20	0.43	27.53	0.51	29.36	0.43	25.24	0.71	90.03	0.86	34.14	0.60
SiO_2	34.59	0.12	42.78	0.63	41.30	0.39	53.63	1.09	-	-	34.96	0.68
Al_2O_3	8.14	0.10	2.67	0.16	2.18	0.07	11.29	0.33	-	-	6.78	0.05
CaO	3.63	0.10	4.82	0.11	4.65	0.08	6.96	0.23	-	-	3.61	0.18
FeO	13.71	0.47	18.08	0.56	17.43	0.68	3.04	1.20	8.29	0.57	19.39	0.43
S	0.05	0.01	0.74	0.03	0.47	0.47	-	-	-	-	0.07	0.01
Total	98.33	0.77	96.63	0.52	95.37	0.83	100.16	1.10	98.32	0.33	98.95	0.19

*: NiO, CoO, V_2O_3, Cr_2O_3, as minor elements

Table S1. Summary of experimental conditions and results by electron microprobe. Standard deviations of multiple measurements are given on the last significant digit in parentheses or in separate columns.

Starting material	MgO	SiO_2	Al_2O_3	CaO	FeO	others	total
pyrolite glass	41.3(8)	41.8(6)	4.6(3)	3.48(8)	8.3(3)	-	99.4(9)
basalt glass	9.3 (1)	48.6(1)	15.3(1)	10.7(1)	10.9(1)	2.25(5)*	97.1(1)
(Mg,Fe)O	81.1(7)	-	-	-	18.4(5)	-	99.5(8)

*: NiO, CoO, V_2O_3, Cr_2O_3, as minor elements

Table S2. Composition of starting materials in wt%, measured by electron microprobe with standard deviations of multiple measurements are shown in parentheses.

Element (*i*)	Mg^{α}	Mg^{β}	Mg^{γ}	O^{δ}	Si^{δ}
a_i	−3.9 (0.2)	−2.8 (1.4)	0.1 (0.1)	0.1 (0.4)	0.6 (0.3)
b_i	0	-4233 (4851)	−10851 (1000)	−2200 (900)	−11700 (800)
c_i	0	54 (50)	0	5 (12)	0
d_i	−18.6 (2.0)	−8.0 (3.7)	0	-7 (3)	-7 (4)*
e_i	0	1.4 (2.9)	-	-	-
f_i	0	1.6 (3.1)	-	-	-

α: This study, fitting parameters *(a* and *d*). Other parameters are found statistically insignificant (P-value > 0.05 for the *F*-test).

β: Fitting results assuming all parameters (*a, b, c, d, e* and *f*) are significant.

γ: From [*O'Rourke and Stevenson*, 2016]

δ: From [*Fischer et al.*, 2015]

*: See more details in [*Fischer et al.*, 2015] for self-interaction terms for Si.

Table S3. Parameters with uncertainties in MgO exsolution model. Exchange coefficient (K_d) is parameterized as function of temperature (T) and pressure (P) as: $\log_{10}K_d=a+b/T+cP/T+d\log_{10}(1-X_O)+e\log_{10}(1-X_C)+e\log_{10}(1-X_S)$. Standard errors (1σ) are in parentheses. Also note that threshold for significance is set to be 2σ, i.e., P value=0.05 in our regression.

Symbol	Value	Units	Reference
α_c	1×10^{-5}	K^{-1}	Thermal expansivity of core
α_x	1.12	nd	Compositional expansivity
c_c	840	J kg^{-1} K^{-1}	Specific heat of core
E_{ic}	300	kJ K^{-1}	Gravitational energy release at ICB
η_c	0.8	nd	Average core to CMB adiabatic temperature drop
γ_{dip}	0.2	nd	Magnetic dipole intensity coefficient in Equ. (16)
L_{ic}	750	kJ kg^{-1}	Latent heat release at ICB
L_e	2.5×10^{-8}	W Ω K^{-1}	Lorentz number
$Q^*_{rad,\ U238}$	7.50	TW	Default present-day BSE U238 power
$Q^*_{rad,\ U235}$	0.34	TW	Default present-day BSE U235 power
$Q^*_{rad,\ Th232}$	8.27	TW	Default present-day BSE Th232 power
$Q^*_{rad,\ K40}$	4.03	TW	Default present-day BSE K40 power
$Q^*_{crad,\ U238}$	0.072	TW	Default present-day core U238 power
$Q^*_{crad,\ U235}$	0.003	TW	Default present-day core U235 power
$Q^*_{crad,\ Th232}$	0.0079	TW	Default present-day core Th232 power
$Q^*_{crad,\ K40}$	3.7	TW	Default present-day core K40 power
ρ_c	11900	kg m^{-3}	Core density
ρ_{ic}	13000	kg m^{-3}	Inner core density
ρ_x	6000	kg m^{-3}	Exsolution density
σ_c	10×10^5	S m^{-1}	Core electrical conductivity
T_{liq1}	3527	K	Liquid coefficient
T_{liq2}	1.85×10^{-10}	K m^{-2}	Liquid coefficient
T_{ad1}	1.41×10^{-10}	K m^{-2}	Liquid coefficient
α_0	3.426999×10^{28}	J/K	Total exsolution energy coefficient
α_1	-2.065620×10^{25}	J/K^2	Total exsolution energy coefficient
α_2	4.190393×10^{21}	J/K^3	Total exsolution energy coefficient
α_3	-2.853338×10^{17}	J/K^4	Total exsolution energy coefficient

Table S4. Model constants. Note: nd, Non-dimensional units; ICB, inner core boundary; BSE, bulk silicate Earth.

References:

Adjaoud, O., G. Steinle-Neumann, and S. Jahn (2011), Transport properties of Mg2SiO4 liquid at high pressure: Physical state of a magma ocean, *Earth and Planetary Science Letters*, *312*(3-4), 463-470.

Akahama, Y., and H. Kawamura (2006), Pressure calibration of diamond anvil Raman gauge to 310 GPa, *J. Appl. Phys.*, *100*(4).

Anzellini, S., A. Dewaele, M. Mezouar, P. Loubeyre, and G. Morard (2013), Melting of Iron at Earth's Inner Core Boundary Based on Fast X-ray Diffraction, *Science*, *340*(6131), 464-466.

Badro, J. Siebert, and F. Nimmo (2016), An early geodynamo driven by exsolution of mantle components from Earth's core, *Nature*, *536*(7616), 326-328.

Badro, J. P. Brodholt, H. Piet, J. Siebert, and F. J. Ryerson (2015), Core formation and core composition from coupled geochemical and geophysical constraints, *Proceedings of the National Academy of Sciences of the United States of America*, *112*(40), 12310-12314.

Barin, I. (1995), *Thermochemical Data of Pure Substances*, VCH, Verlagsgesellschaft, Weinheim, Germany.

Chidester, B. A., Z. Rahman, K. Righter, and A. J. Campbell (2017), Metal-silicate partitioning of U: Implications for the heat budget of the core and evidence for reduced U in the mantle, *Geochimica et Cosmochimica Acta*, *199*, 1-12.

de Koker, N., G. Steinle-Neumann, and V. Vlcek (2012), Electrical resistivity and thermal conductivity of liquid Fe alloys at high P and T, and heat flux in Earth's core, *Proceedings of the National Academy of Sciences of the United States of America*, *109*(11), 4070-4073.

Deng, J., Z. Du, L. R. Benedetti, and K. K. M. Lee (2017), The influence of wavelength-dependent absorption and temperature gradients on temperature determination in laser-heated diamond-anvil cells, *J. Appl. Phys.*, *121*(2), 11.

Deng, L., Y. Fei, X. Liu, Z. Gong, and A. Shahar (2013), Effect of carbon, sulfur and silicon on iron melting at high pressure: Implications for composition and evolution of the planetary terrestrial cores, *Geochimica et Cosmochimica Acta*, *114*, 220-233.

Driscoll, and D. Bercovici (2014), On the thermal and magnetic histories of Earth and Venus: Influences of melting, radioactivity, and conductivity, *Phys. Earth Planet. Inter.*, *236*, 36-51.

Du, Z., and K. K. M. Lee (2014), High-pressure melting of MgO from (Mg,Fe)O solid solutions, *Geophysical Research Letters*, *41*(22), 8061-8066.

Du, Z., T. Gu, V. Dobrosavljevic, S. T. Weir, S. Falabella, and K. K. M. Lee (2015), Using stepped anvils to make even insulation layers in laser-heated diamond-anvil cell samples, *Review of Scientific Instruments*, *86*(9).

Dubrovinskaia, N., et al. (2005), Beating the miscibility barrier between iron group elements and magnesium by high-pressure alloying, *Phys. Rev. Lett.*, *95*(24), 4.

Fei, Y., C. Murphy, Y. Shibazaki, A. Shahar, and H. Huang (2016), Thermal equation of state of hcp-iron: Constraint on the density deficit of Earth's solid inner core, *Geophysical Research Letters*, *43*(13), 6837-6843.

Fiquet, G., A. L. Auzende, J. Siebert, A. Corgne, H. Bureau, H. Ozawa, and G. Garbarino (2010), Melting of Peridotite to 140 Gigapascals, *Science*, *329*(5998), 1516-1518.

Fischer, R. A., Y. Nakajima, A. J. Campbell, D. J. Frost, D. Harries, F. Langenhorst, N. Miyajima, K. Pollok, and D. C. Rubie (2015), High pressure metal-silicate partitioning of Ni, Co, V, Cr, Si, and O, *Geochimica et Cosmochimica Acta*, *167*, 177-194.
Gu, T., M. Li, C. McCammon, and K. K. M. Lee (2016), Redox-induced lower mantle density contrast and effect on mantle structure and primitive oxygen, *Nature Geoscience*, *9*(9), 723-727.
Huang, H., Y. Fei, L. Cai, F. Jing, X. Hu, H. Xie, L. Zhang, and Z. Gong (2011), Evidence for an oxygen-depleted liquid outer core of the Earth, *Nature*, *479*(7374), 513-516.
Karki, B. B. (2010), First-Principles Molecular Dynamics Simulations of Silicate Melts: Structural and Dynamical Properties, in *Theoretical and Computational Methods in Mineral Physics: Geophysical Applications*, edited by R. Wentzcovitch and L. Stixrude, pp. 355-389, Mineralogical Soc Amer, Chantilly.
Karki, B. B., J. Zhang, and L. Stixrude (2013), First principles viscosity and derived models for MgO-SiO2 melt system at high temperature, *Geophysical Research Letters*, *40*(1), 94-99.
Landeau, M., P. Olson, R. Deguen, and B. H. Hirsh (2016), Core merging and stratification following giant impact, *Nature Geoscience*, *9*, 786-789.
Liu, J., J. Li, and D. Ikuta (2016), Elastic softening in Fe_7C_3 with implications for Earth's deep carbon reservoirs, *Journal of Geophysical Research-Solid Earth*, *121*(3), 1514-1524.
Ma, Z. (2001), Thermodynamic description for concentrated metallic solutions using interaction parameters, *Metall. Mater. Trans. B-Proc. Metall. Mater. Proc. Sci.*, *32*(1), 87-103.
O'Rourke, J. G., and D. J. Stevenson (2016), Powering Earth's dynamo with magnesium precipitation from the core, *Nature*, *529*, 387-389.
Olson, P., and U. R. Christensen (2006), Dipole moment scaling for convection-driven planetary dynamos, *Earth and Planetary Science Letters*, *250*(3-4), 561-571.
Posner, E. S., D. C. Rubie, D. J. Frost, V. Vlcek, and G. Steinle-Neumann (2017), High P-T experiments and first principles calculations of the diffusion of Si and Cr in liquid iron, *Geochimica et Cosmochimica Acta*, *203*, 323-342.
Pozzo, M., C. Davies, D. Gubbins, and D. Alfe (2012), Thermal and electrical conductivity of iron at Earth's core conditions, *Nature*, *485*(7398), 355-358.
Prakapenka, V. B., A. Kubo, A. Kuznetsov, A. Laskin, O. Shkurikhin, P. Dera, M. L. Rivers, and S. R. Sutton (2008), Advanced flat top laser heating system for high pressure research at GSECARS: application to the melting behavior of germanium, *High Pressure Research*, *28*(3), 225-235.
Rubie, D. C., D. J. Frost, U. Mann, Y. Asahara, F. Nimmo, K. Tsuno, P. Kegler, A. Holzheid, and H. Palme (2011), Heterogeneous accretion, composition and core-mantle differentiation of the Earth, *Earth and Planetary Science Letters*, *301*(1-2), 31-42.
Smith, E. M., S. B. Shirey, F. Nestola, E. S. Bullock, J. Wang, S. H. Richardson, and W. Wang (2016), Large gem diamonds from metallic liquid in Earth's deep mantle, *Science*, *354*(6318), 1403-1405.
Steelmaking, J. S. f. t. P. o. S. a. t. N. C. o. (1988), *Steelmaking Data Sourcebook*, 273-297 pp., Gordon and Breach Science Publishers, New York.

Suer, T.-A., J. Siebert, L. Remusat, N. Menguy, and G. Fiquet (2017), A sulfur-poor terrestrial core inferred from metal–silicate partitioning experiments, *Earth and Planetary Science Letters*, *469*, 84-97.
Tsuno, K., D. J. Frost, and D. C. Rubie (2011), The effects of nickel and sulphur on the core-mantle partitioning of oxygen in Earth and Mars, *Phys. Earth Planet. Inter.*, *185*(1-2), 1-12.
Tsuno, K., D. J. Frost, and D. C. Rubie (2013), Simultaneous partitioning of silicon and oxygen into the Earth's core during early Earth differentiation, *Geophysical Research Letters*, *40*(1), 66-71.
Wade, and B. J. Wood (2005), Core formation and the oxidation state of the Earth, *Earth and Planetary Science Letters*, *236*, 78-95.
Wade, J., and B. J. Wood (2012), Metal-silicate partitioning experiments in the diamond anvil cell: A comment on potential analytical errors, *Phys. Earth Planet. Inter.*, *192*, 54-58.
Wahl, S. M., and B. Militzer (2015), High-temperature miscibility of iron and rock during terrestrial planet formation, *Earth and Planetary Science Letters*, *410*, 25-33.